Journal Title
XX(X):2–40

DOI: 10.1177/ToBeAssigned
www.sagepub.com/
SAGE

Aerodynamic effects of surface deformities on aerofoils for low speed stratospheric flight

Jeremy Kimmons[1], Peter Thomas[2], and Simone Colonia[3]

Abstract

High-altitude pseudo satellites are an expanding focal area of the aerospace industry which require new technologies and manufacturing processes to reduce weight and increase efficiency with the aim of increasing endurance. One such process has resulted in the occurrence of small deformities along the leading-edge of a lightweight unmanned aerial vehicle structure with the application of its skin, which may have a detrimental impact on its performance and efficiency. This paper focuses on the effects of these manufacturing deformities on the aerodynamic performance of the vehicle's aerofoil when operating in low Reynolds number flow with the intention of identifying any detrimental flow variation. This analysis is achieved by comparing the lift curve, drag polar and pressure coefficient of both the deformed and undeformed cases of two aerofoils: a SG6042 and a GOE 523. This is accompanied with an examination of the local flow conditions scrutinising the near wall y^+ and turbulent kinetic energy calculations. The investigation finds that in two-dimensional flow, the deformities replicate the effects of transition trips in the shrinking or elimination of laminar separation bubbles. At Reynolds numbers below 250,000, the deformities reduce the net drag while leaving the lift largely unaffected. However, as a result there is a slight shift in the minimum power condition in the order of 8% which would produce some performance loss for power efficiency and endurance.

Keywords

High-Altitude Pseudo Satellite, Aerofoil, Surface deformation, CFD, k-kl-ω, Laminar separation bubble.

1. Introduction

High-Altitude Long Endurance (HALE) and High-Altitude Pseudo Satellite, or High-Altitude Platform Station, (HAPS) concepts are not new to the aerospace industry, yet still present serious challenges to those who seek to operate them within the stratosphere. HAPS are likely to be Unmanned Air Systems (UAS) employed in a surveillance or telecommunications role and are required to remain in the stratosphere for long durations. Accordingly, in the absence of other viable sources, they currently utilise solar energy to power their systems and recharge batteries.

The ability to maintain altitude in the stratosphere during the night is limited by the power density of the storage system and the aerodynamic efficiency of the platform as it is forced to rely purely on battery power with little to no solar exposure. As such, the platform's weight is therefore a key aspect that contributes to the aerodynamic efficiency due to the relationship between weight and lift. One of the techniques used to keep the weight down is to have a lightweight wing covering, or skin, that is bonded onto the aerostructure. However, current manufacturing processes can lead to deformations on the skin which raises questions for the effect on the aerodynamic efficiency of the finished wing.

1.1. Skin surface deformation

Biaxially-oriented Polyethylene Terephthalate (BoPET), more often known by the trade name Mylar, is a lightweight material commonly used to skin remote control aircraft. During application of these coverings, the Mylar is pulled over the wing section and bonded down, usually using an adhesive which requires a heat or ultraviolet source to cure. This allows time for the Mylar to be applied and wrinkles to be pressed out before the glue is set. Once the glue has set, the skin can then be tensioned using a heat gun to contour the ribs and create the wing profile. This process works well when the covering is

[1]Airbus Defence and Space Limited, Stevenage, SG1 2AS, UK
[2]Centre for Engineering Research, University of Hertfordshire, Hatfield, UK, AL10 9AB
[2]Airbus Defence and Space Limited, Farnborough, GU14 6FF, UK

Corresponding author:
Peter Thomas, Centre for Engineering Research, University of Hertfordshire, Hatfield, UK, AL10 9AB.
Email: p.thomas5@herts.ac.uk

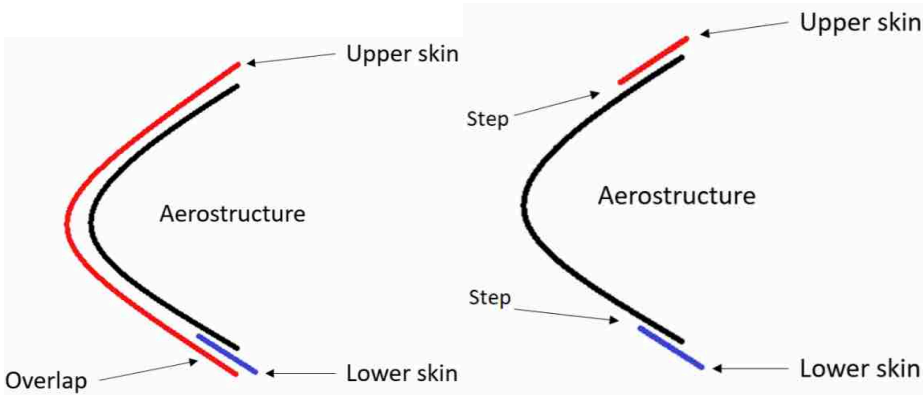

(a) Upper skin overlap. **(b)** Skin step.

Figure 1. Skin wrapping discontinuities.

applied around the whole wing, encompassing the leading-edge. However, in those cases where it is undesirable/unfeasible to apply the Mylar around the whole wing section (for example where the structure is large, fragile or the camber too great) the Mylar may be applied from the leading edge to the trailing edge on both the upper and lower surfaces of the aerofoil independently. In this situation there is either an overlap of the skin as in Figure 1a resulting in a backward facing step, or the skin is terminated on the leading-edge structure without an overlap, creating two forward facing steps (Figure 1b). With this process, deformities in the form of raised ridges, illustrated in Figure 2, can occur in both scenarios. In the case of an overlap the deformities are more likely to occur on the underside of the aerofoil where the upper skin bonds to the lower; this presents less of a defect to the airflow as opposed to that which is seen in the case of the two forward facing steps of Figure 1b.

The defects illustrated in Figure 2 have been identified almost exclusively in the vicinity of the leading-edge, specifically along the bond-line between the wing covering and the leading-edge structure where the manufacturing process involves the skin being ended off. The deformities appear as several ridged lines and are partly due to the processes involved in applying the wing covering. Although in this case the deformities mostly align with the longitudinal axes of the structure, there are occasions where the shape or angle can present a more severe angled or even radial path near to the leading-edge. Deformities can be seen to continue occurring as far back as 25% of the chord where leading-edge structures terminate. There is no predefined characteristic which

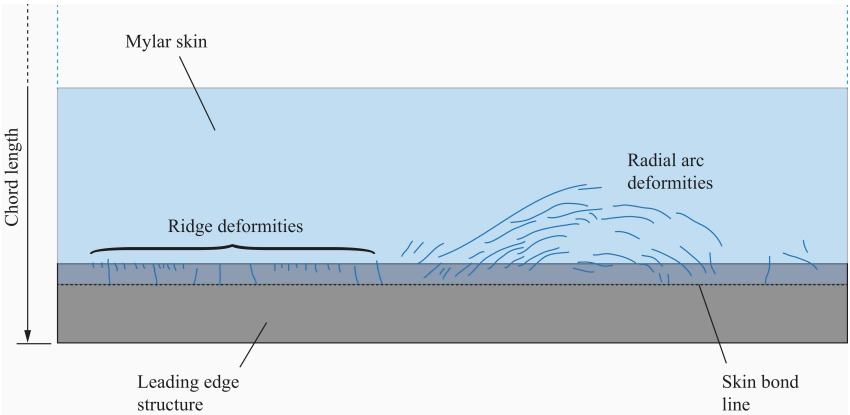

Figure 2. Sketch of part of a HAPS wing with the raised leading-edge skin deformities at or near the skin bond-line.

may model how these deformities will shape during the manufacturing process and this presents a significant challenge in terms of modelling them for study.

The effect of these deformities on the aerodynamics in flight is yet to be thoroughly discussed in the relevant literature. It is assumed that this will be a negative effect. However, at low Reynolds numbers, a trip (such as a step or ramp) can be of benefit to the aerodynamic performance of an aerofoil[1]. At high altitudes, where HAPS are designed to operate, the atmospheric characteristics which positively contribute to aerodynamic performance of aerofoils at low altitudes are severely impinged[2]. The lift and drag equations,

$$L = \frac{1}{2}\rho V^2 S C_L, \quad \text{and} \quad D = \frac{1}{2}\rho V^2 S C_D,$$

feature two variables which will be intrinsically low for a HAPS in nominal cruise conditions: the atmospheric air density, ρ and its true airspeed, V. The atmospheric density in the stratosphere is a fraction of that seen at sea level. At an ISA altitude of 70,000 ft, $\rho = 0.0709$ kg/m^3, less than 5.8% of the sea level value (1.2256 kg/m^3). HAPS cruise at relatively low speed due to the limited power available for thrust. This implies a low value of V and, as a squared term in the aerodynamic force equations, it has a significant impact on the generation of both lift and drag. As compensation for this, HAPS must feature high lift aerofoils with inherently low drag to maintain efficient cruise and altitude[3]. This is achieved through aerofoil optimisation with the goal of attaining a high coefficient of lift, C_L and low coefficient of drag, C_D (i.e. high lift-to-drag ratio, L/D) by the manipulation of aerofoil geometry. The key target for HAPS aerodynamic

efficiency is to operate at the minimum power condition, this is achieved by maximising the value of $C_L^{3/2}/C_D$ [4].

1.2. Existing work

The operating altitude of the HAPS UAS varies between 60,000 ft and 70,000 ft, with a spanwise Reynolds numbers range from 100,000 to 300,000. Considerable research has been conducted with aerofoils at low Reynolds numbers ($\mathrm{Re} \leq 500,000$) much of which has come out of the University of Illinois'low-speed aerofoil testing (see, for example, Ref. 5). Many of these studies show aerofoils are highly sensitive to changes in Reynolds number and highlight a flow phenomenon known as laminar separation bubble (LSB) which can greatly increase drag, be utilised to benefit maximum lift [6], or create the conditions for a leading-edge stall [7]. The performance of high-lift, low-speed aerofoils has been identified to drop significantly due to laminar separation at $\mathrm{Re} \leq 100,000$ [8]. The chordwise dimension of the bubble is greatly affected by Reynolds number and its chordwise position by angle of attack [9]. Separation bubbles can be controlled by triggering transition from laminar to turbulent flow which can shift re-attachment towards the leading-edge [10]. Methods of triggering transition include the introduction of a step or ramp into the aerofoil boundary layer [1,8,11]. Transition can also be delayed by the influence of heating elements, thereby increasing the Reynolds number associated with transition [12]. Similar techniques can be employed to enhance the maximum lift of an aerofoil without the use of devices that protrude into the boundary layer [13].

In their catalogued work Lyon et al. [8] also discuss the impact of triggering transition on a SG6042 aerofoil with a spanwise zigzag trip, located at 2% and 5% of the chord on the upper and lower surfaces respectfully. While this method has the effect of mitigating the undesirable drag additions of the LSB at low Reynolds numbers, it brings with it an increase in skin friction which results in increased drag. It was proposed that fixing transition near the leading edge will provide a net benefit in reducing drag when operating around Re = 100,000. However, Lyon et al. also note that trip heights greater than 0.04% of the chord result in the swift deterioration of the aerofoil performance. An interesting point to highlight is that the angle of attack which correlates with the maximum lift to drag ratio remains constant with the application of the trigger mechanism. Giguère & Selig [14] investigated the effects of leading-edge tape on the aerodynamic performance of several aerofoils at low Reynolds numbers. A 0.2 mm thick tape was wrapped around the leading- edge. The upper surface was tested in three configurations; 5%, 15% and 30% of the chord and in all cases, the lower surface received a covering of 5% chord.

For low values of Reynolds number, the tape provided a large boost in the lift to drag ratio and this increased with higher percentage upper surface coverage. The benefits are lost at higher Reynolds numbers where the tape only contributes to the increase of drag. Giguère & Selig liken an increase in tape thickness to an increase in Reynolds number because they both relate to a change in the boundary layer thickness.

Salim & Cheah[15] used Ansys Fluent to investigate the effects of a ridge protruding into the boundary layer on a flat plate and its effects on y^+, the dimensionless value of the near-wall viscous layer. They discuss how the ridge would result in a spike in y^+ when plotted against x/c and in conclusion advise against attempting to resolve the buffer layer as there were no viscous models capable of accurately predicting flow in this regime. Salim & Cheah describe y^+ as having a significant effect on the skin friction coefficient (a useful tool in assessing laminar-turbulent transition). There are three y^+ regions of note: the viscous sublayer, the buffer layer and the fully turbulent layer. They go on to map these regions as $y^+ < 5$, $5 < y^+ < 30$, and $y^+ > 30$ respectively. From Salim & Cheah's study it can be seen that boundary layers resolved within the buffer layer ($5 < y^+ < 30$) result in less accurate coefficients of friction being recorded.

Generally, transition trips have been shown to positively augment low Reynolds number flow over aerofoils, seeing reductions in the size or elimination of the LSB. However, no research has specifically targeted manufacturing deformities along or near the leading edge.

1.3. Paper outline

This paper investigates the aerodynamic effect of the observed deformities on the skin of the HAPS wings through numerical simulations using Ansys Fluent[16]. Experimental validation is undertaken using existing empirical data from Ref. 8 as well as wind tunnel testing. In the next section the characteristics of the deformities are discussed and an approach to modelling them is established. In §3 the computational fluid dynamics (CFD) setup in Fluent is described, with particular discussion around the choice of viscous model for transitional flow and the use of a structured and unstructured mesh. Results from the CFD work are then presented in §4. Section 5 presents a comparison of experimental wind tunnel tests with results obtained from the CFD modelling approach discussed in §3. The paper is concluded in §6.

Table 1. Mean observed dimensions of deformities (percent of chord).

Characteristic	Ridge ($\%c$)	Arc ($\%c$)
First occurrence	2.778	3.333
Height	0.056	0.056
Width	0.111	0.111
Length	0.556	-
Minimum diameter	-	2.444
Maximum diameter	-	4.444

2. Methodology

2.1. Modelling the deformities

A deformity can be defined as any wrinkle in the skin presenting a profile with a height greater than the thickness of the skin itself. Visually scanning the wing's leading edge enabled a range of deformities to be detected which were imaged for analysis. The bond-line indicated in Figure 2 generally contains the highest density of deformities. The deformities observed can be categorised by appearance as either 'Ridge' or 'Arc' deformities and their geometric characteristics are tabulated in Table 1. Figure 2 gives an indication of the frequency at which the deformities can occur along the leading edge. Ridges straddling 100% of the bond line, as well as smaller ridges extending 20 to 50% of the bond line, could occur.

Two methods were looked at for modelling the deformity on the aerofoil:

1. *Coordinate manipulation:* The baseline coordinates for the aerofoil were directly altered to model the required deformity size. It is important to note that the ridge is a separate set of coordinates on top of the aerofoil, this is due to the deformity presenting a flat face to the oncoming flow and not incorporated into the spline of the aerofoil profile; this mimics the form observed during manufacture.
2. *3D projection:* The aerofoil was profiled first in CAD modelling software by importing the baseline undeformed coordinates. A sketch of the deformity can then be projected onto the surface and extruded to the required height in accordance with Table 3-1. The extrusion is then closed and the ridge deformity is fully formed. The model can then imported into CFD software to use as either a 2D or 3D section.

Since a 2D projection of an arc deformity will result in a ridge, the analysis in this paper has been restricted to ridge deformities.

2.2. Description of aerofoils

Two aerofoil sections were used in this study. First, the SG6042 (Figure 3a) is a high performance aerofoil typical of HAPS UAS. The aerofoil has good lift to drag characteristics[17] and was designed to maintain a high lift to drag ratio between the coefficients of lift 0.6 and 1.2 for Reynolds numbers ranging 250,000 to 500,000. The SG6042 was used in the initial CFD analysis.

Second, a wind tunnel test model with a GOE 523 aerofoil was made available. Due to its high lift to drag ratio and large surface area, the GOE 523 section (Figure 3b) gives a performance comparable to the desired characteristics of a HAPS aerofoil. The wing model has equal chord and span of 0.5 m, giving an aspect ratio of $A_R = 1$.

3. CFD modelling

3.1. Aerofoil model

Aerofoils are generally presented in coordinate form and need to be converted to 2D surfaces or 3D solid models to enable CFD to be performed on them. The aerofoils can also be listed with fewer data points than may be desired. For example, a typical SG6042 aerofoil datafile available online consists of 81 data points to form the full profile. This was increased to 300 points using XFOIL's[18] interpolation routines. By increasing the resolution of the profile, the location of maximum thickness and camber is very slightly altered, though this is assumed to have very minimal effect overall. The higher resolution aerofoil coordinates were then imported into the design modeller module within Ansys so that the fluid domain could be constructed around the aerofoil. To assist in the structuring of the mesh later, an arc inlet was created to approximately mirror the curvature of the leading edge[19].

3.2. Domain sizing

When using a computational approach to solve aerodynamic flow problems, the free stream far-field must be established. This can be represented by a number of geometries such as a rectangular, inverse D, O-domain shape, etc. The key is the size of the domain; generally a large domain has more mesh cells and requires longer computation time and

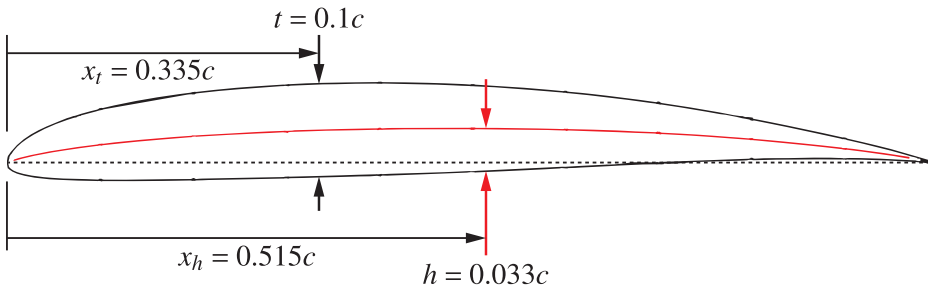

(a) SG6042.

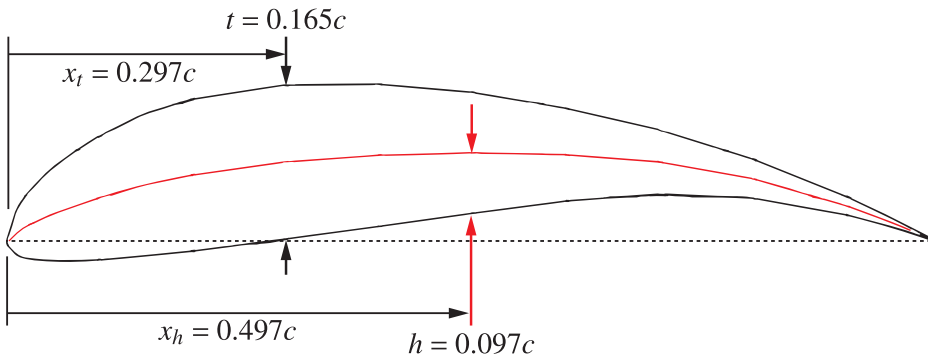

(b) GOE 523.

Figure 3. The high lift aerofoil sections investigated. Maximum thickness and maximum camber locations are indicated.

therefore increased cost. The aim is to keep the domain as small as possible without resulting in adverse effects such as downstream vorticity reflections or wall boundary layer interference[20].

There are widely varied opinions regarding the correct sizing of the computational domain. This is typically identified iteratively through trial and error. In the case of an aerofoil, the size of the domain is measured in multiples of the chord. Domain sizes typically seen in literature sit between $20c$ and $30c$ downstream of the aerofoil trailing edge, this represents the largest portion of the domain for a rectangular or D shape or, in the case of an O-domain, its radius[21,22].

Bose et al.[23] utilised a rectangular domain with a structured mesh surrounding the aerofoil inflated to fully encompass the boundary layer whilst the far field comprised an unstructured mesh of triangles. Through a series of iterations, they show that the number

of divisions around the aerofoil required to converge their results is 200. By reducing the amount of divisions surrounding the aerofoil, the computation time can be reduced. Interestingly though, they opt for a $15c$ downstream wake field, smaller than that used by many previous studies, and incorporate a rather large upper and lower wall distance of $9c$.

Sørensen, et al.[24] describe several types of mesh that they refer to as O-mesh, C-H mesh and OCH-mesh. During their study seven partners ran the same parameters through their respective institutions' CFD solvers, all seven solvers produced different results even though the majority used the same mesh configuration. This implies that the selected viscous model for this project will certainly have an impact on the results compared with those that may be obtained by other solvers. A suggestion made that may remove the inconsistencies seen between different CFD codes seen was to increase the domain size to $100c$[24]. However, for the scope of most small-scale studies a $100c$ domain would require excessive computational time and was therefore not used here. Instead, the domain was sized at $20c$ based on the work of Bose et al.[23], who showed that a smaller domain ($15c$ downstream wakefield) produces sufficiently accurate results. The domain consists of a leading $4c$ region in front of the aerofoil and $15c$ aft with $4c$ above and below as can be seen in Figure 4. Initial simulations showed that the $4c$ spacing between the aerofoil and the inlet and slip boundary showed no impact to the results. The domain is smaller than the $20c$ or $30c$ downstream lengths commonly seen in literature, however this is owing to the lower velocities that are being investigated which allow a smaller domain to be utilised for lower Reynolds numbers[20]. Several lines were also drafted onto the domain which form 'connectors' that are used to form a structural guide for the mesh to follow; this will enable a higher resolution mesh to be achieved around the aerofoil. The connectors near the leading edge extend from a point placed $0.04c$ inside the aerofoil along its chord line to the edge of the domain. The connectors aft of the aerofoil extend from the trailing edge construction point to the edge of the domain.

3.3. Turbulence model

With consideration to the CFD package chosen for this work (Fluent), there are several sub-models available for turbulent and transitional flow. Since the laminar bubble separation can induce transition to turbulent flow, the choice of model is reduced to turbulent and transition. The selection can be further reduced to that of the transition models, as the deformities will likely impact how and when transition occurs. This is

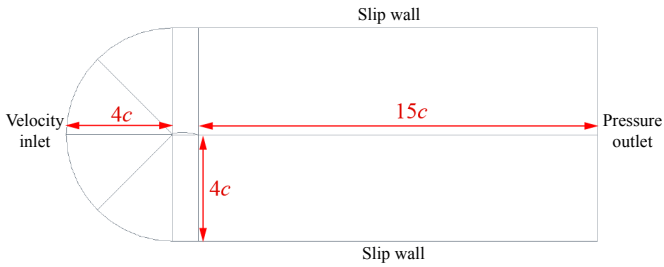

Figure 4. 20c D-domain. Connectors shown are for a structured mesh.

based on the understanding developed with the variety of trips and triggers used by the various studies in the literature [1,8,11].

Two widely used transition models are the three-equation k-kl-ω [25] and the four equation γ-Re_θ [26]. The first model (k-kl-ω) is more associated with the generation of turbulent kinetic energy within the boundary layer, the three terms being turbulent kinetic energy, k, laminar kinetic energy, kl, and specified dissipation rate, ω. The second model (γ-Re_θ) focuses on boundary layer thickness and the critical Reynolds number for which intermittency begins to increase, where the intermittency is a scale from zero to one, zero being fully laminar flow and one being fully turbulent. It is noted that the γ-Re_θ model has been modified "to improve the predictions of separated flow transition" [27]. Aftab, et al. [28] state that the k-kl-ω model gives very good results at low incidence angles. However, they rejected its use for further study due to the increased computational time compared to the γ-Re_θ method. This is interesting because k-kl-ω is formed of fewer equations, therefore one would expect this to result in faster simulation. Equally, it has also been stated that the two models produce comparable results [29].

An initial comparison was conducted between the k-kl-ω and γ-Re_θ transition models, the results of which are illustrated in Table 2. It was seen that identifying transition was more straightforward with γ-Re_θ, where an intermittency contour plot would clearly show where the model predicted transition. On the other hand, the k-kl-ω would require interpretation of the laminar-turbulent contours coupled with an x-velocity investigation. The γ-Re_θ model, however, had much longer computation times than k-kl-ω, which produced a more reasonable c_l in line with empirical data. The difference in the values of c_d between the two methods was relatively small. Due to the volume of simulations required, and the better match with the empirical data, the k-kl-ω model was selected. The k-kl-ω model is used with the Reynolds-averaged Navier-Stokes (RANS) equations

Table 2. Comparison of turbulent models, panel method (XFOIL), and existing empirical data[8], with a SG6042 aerofoil (Re = 10^5, $\alpha = 0^\circ$).

Property	k-kl-ω	γ-Re_θ	XFOIL	XFOIL	Empirical
Turbulent intensity	0.1%	0.1%	Ncrit = 9	Ncrit = 6	$< 0.1\%$
c_l	0.2963	0.2021	0.2637	0.3680	0.311
c_d	0.02115	0.02130	0.02258	0.01773	0.0230
c_l/c_d	14.011	9.4912	11.678	20.76	13.52

and the Ansys Fluent Theory Guides should be consulted for the details on the equations used.

3.4. Near-wall modelling and y^+

Turbulent modelling may require a near wall model to be coupled with it to resolve the laminar-turbulent boundary layer near the target wall. For some models it is desired that $y^+ \leq 1$ in the first layer of the near wall mesh to enable accurate predictions; Kožíšek, et al.[29] maintain a y^+ value of less than one when implementing the k-kl-ω transition model throughout their study. The actual dimension of the first layer of the mesh is termed Δy, where Δy is the height of the first layer and a function of y^+. Estimating Δy is required so that the first mesh is theoretically set up for the required y^+ to resolve the boundary layer in the viscous sublayer and not the buffer layer. y^+ can be calculated from

$$y^+ = \frac{\rho U_\tau \Delta y}{\mu}, \tag{1}$$

where U_τ is the shear velocity. Using (1), for Re = 100,000, the estimated Δy is calculated to be 0.1857 mm.

3.5. Structured mesh

Generally, a structured mesh is more frequently used in the literature as it offers a reduction in computational time compared to unstructured meshes and enables a greater level of selectivity with respect to the y^+ value. The mesh can be constructed with a set of bias conditions to increase the resolution in a certain area of the domain, such as around the aerofoil profile.

The domain was structured according to Figure 5a, showing the split zones set up which are face meshed with quadrilaterals (as opposed to triangles). Bias allocations were then used on the mesh support lines to focus a high density of mesh elements around the aerofoil and the centre of the domain. Of the several bias type options that are available,

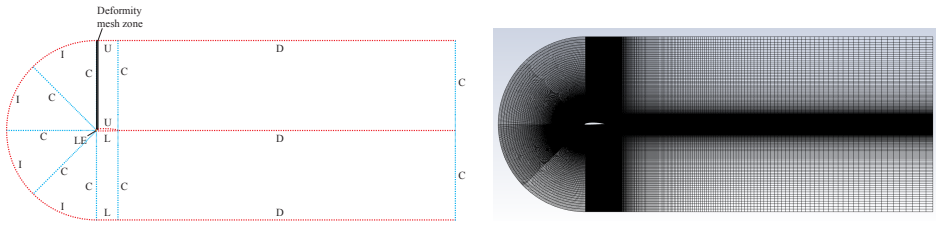

(a) Structural and domain elements. **(b)** Mesh.

Figure 5. Structured domain and mesh.

a logarithmic bias was used; this creates larger spacing between the elements near the far field where the flow is not directly interacting with the aerofoil.

The results of a mesh dependency study with the structured mesh are displayed in Table 3. Test results are shown for increasing mesh divisions, first on domain structural elements that effectively follow the aerofoil surface (all elements in Figure 5a except those labelled C), and then to those effectively normal to the aerofoil surface (the mesh support connectors). Evidently, mesh density in the normal direction is important in ensuring a reliable solution as convergence was faster with more divisions applied along the support connectors. Greater divisions here were also required to obtain y^+ values below 1. The two dimensional lift and drag coefficients, c_l and c_d, converged to 1% error with 500 divisions and a value of $y^+ < 1$ achieved across the aerofoil suggests a satisfactorily detailed mesh. In practice though it is not efficient to use such a globally dense mesh. The mesh size around the connectors was retained whilst the upstream and downstream mesh density were reduced whilst checking for convergence of c_l and c_d and satisfactory y^+ values. The mesh settings chosen (Table 4) result in the structured mesh seen in Figure 5b, with a first layer height of 0.1 mm surrounding the aerofoil. This is approximately two times smaller than the estimated requirement for Δy to give a $y^+ \leq 1$. At approximately 0.15 m from the aerofoil surface, the layer height increases to 2 mm.

In the case of the deformed aerofoil, the mesh settings applied to clean aerofoil above are then altered slightly to accommodate the deformity. A new zone is created which is termed the deformity mesh zone (indicated in Figure 6). Either side of the deformity, the two vertices have their number of divisions retained at 500. The resulting additional meshing for the deformity is shown in Figure 6. It is worth noting that the contact area of the deformity's upper surface has been split into 90 divisions to assist in flow visualisation.

Table 3. Structured mesh dependency results using the k-kl-ω model (Re = 10^5, $\alpha = 0^\circ$).

# Divisions						
Contour	Normal	c_l	Δc_l (%)	c_d	Δc_d (%)	Comments
100	100	0.39153	-	0.01823	-	$y^+ > 3.5$
200	100	0.38339	2.0878	0.01738	4.6694	$y^+ > 3.5$
300	100	0.30861	19.5044	0.02281	31.2608	$y^+ > 3.5$
400	100	0.30067	2.5731	0.02284	0.1181	$y^+ > 3.5$
500	100	0.30680	2.0389	0.02344	2.6489	$y^+ > 3.5$
100	200	0.39832	1.73384	0.01759	3.50328	$y^+ > 1.5$
100	300	0.42436	6.5379	0.01552	11.7431	$y^+ > 1$
100	400	0.41401	2.4378	0.01549	0.2283	$y^+ < 1$
100	500	0.41056	0.8331	0.01561	0.8146	$y^+ < 1$

Table 4. Properties of the structured mesh

Element	ID	# Divisions	Bias factor
Mesh support connectors	C	500	600
Downstream connectors	D	100	600
Upper aerofoil	U	400	No bias
Lower aerofoil	L	400	No bias
Aerofoil leading edge	LE	100	No bias
Inlet	I	100	No bias

3.6. Unstructured mesh

Contrastingly with a structured mesh, an unstructured mesh is substantially faster to create. Unstructured meshes usually require a higher density mesh to achieve acceptable results and when created with quadrilaterals, can compare well to structured meshes[30]. However, unstructured meshes do not require mesh guides in the domain geometry to support the mesh generation. Instead, the mesh can be generated through an automatic method and further sizing constraints can be added later. The automatic method in Ansys was selected with the quadrilaterals dominant option. The base element size was set at 0.1 m. Division sizing of the aerofoil surface was set to 400 on each upper and lower surface and an inflation was applied to the aerofoil surface to inflate the boundary. The inflation started with a first layer thickness of 0.1 mm (to satisfy the calculated y^+ value) and was inflated to 60 layers at a growth rate of 1.07. Figure 7 shows the unstructured mesh around the aerofoil with refinement of the inflation layers.

To establish an appropriate unstructured mesh for the study, a further mesh dependency study was undertaken. Table 5 shows that the mesh with 60 inflation layers is sufficiently

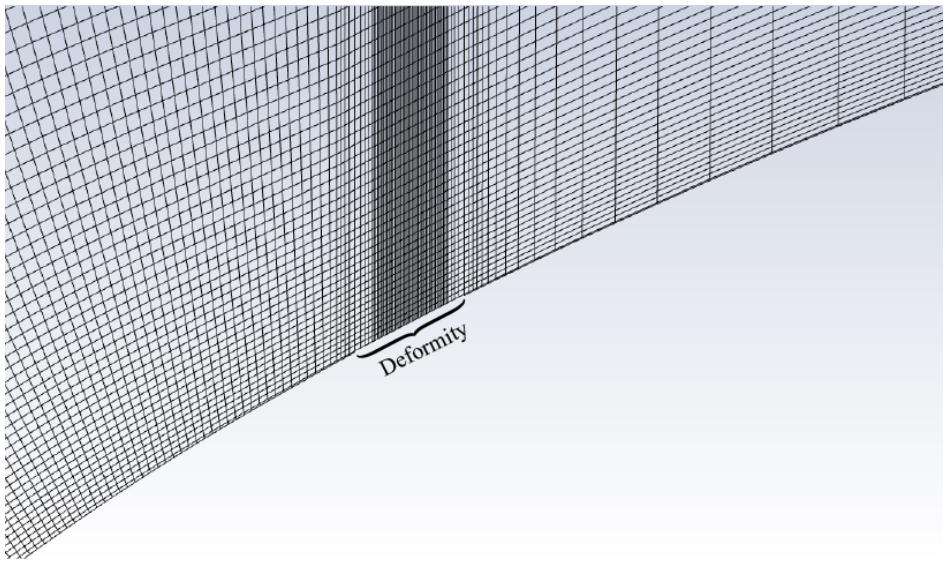

Figure 6. Meshed ridge deformity on SG6042.

Table 5. Unstructed mesh dependency results using the k-kl-ω model (Re = 100,000, $\alpha = 0^{\circ}$).

Inflation layers	c_l	Δc_l (%)	c_d	Δc_d (%)	Comments
20	0.34962	-	0.01922	-	$y^+ < 1$
30	0.40461	15.7283	0.01611	16.1852	$y^+ < 1$
40	0.33490	17.2307	0.02192	36.0905	$y^+ < 1$
50	0.31170	6.9255	0.02081	5.0585	$y^+ < 1$
60	0.30923	0.7929	0.02083	0.0783	$y^+ < 1$

converged with an error percentages of 1%. The y^+ value remained below 1 at all inflation layers so 60 inflation layers were ultimately chosen.

3.7. Choice of mesh approach

In order to achieve a satisfactory y^+ value across the aerofoil when using a structured mesh a considerably more dense mesh was required than when using an unstructured mesh. As a result, it was found in this study that a structured mesh required considerably more computational time than the unstructured mesh. Also, when undertaking the analysis, it was more convenient when performing angle of attack sweeps to parameterise

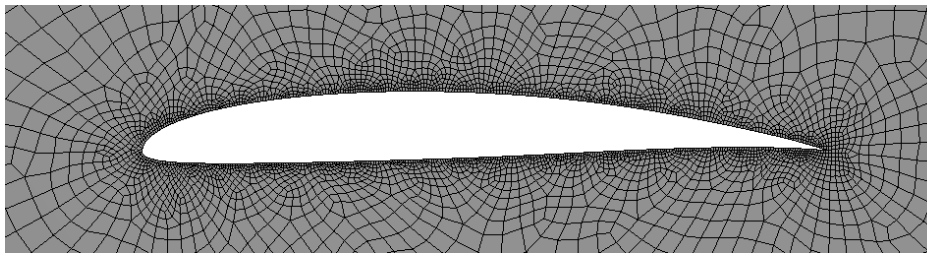

(a) No inflation.

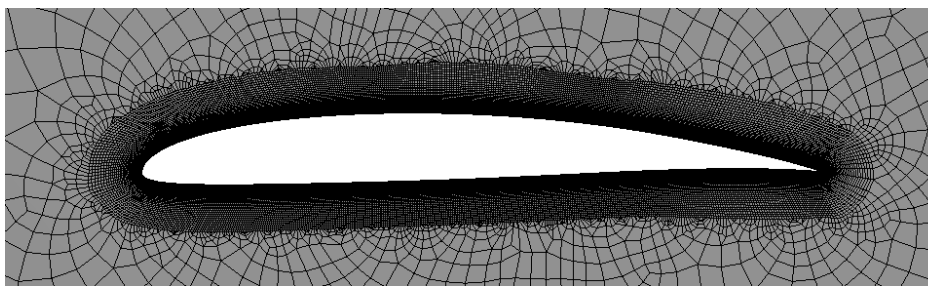

(b) 60 layers for inflation, 1.07 growth rate.

Figure 7. Different near-wall cell density in the unstructured mesh.

the angle of rotation of the aerofoil geometry in Ansys Workbench. For this, the unstructured mesh is more suited since the structured mesh would require individual mesh support lines for each incidence angle. Furthermore, comparing Table 3 and Table 5 indicates that the unstructured mesh results we closer to the experimental results from Ref. 8 ($c_l = 0.311$, $c_d = 0.0230$). Convergence to the residual tolerance (0.001) was also noticeably faster with the unstructured mesh. On this basis the unstructured mesh with the k-kl-ω model was used for the analysis.

4. CFD results

4.1. Setup

Ansys Fluent was initialised in 2D with double precision. Table 6 displays the settings used. All other settings were left as their default values. Both the gradient and pressure-velocity coupling variables were left as standard. All equation variables were calculated as second order (up from first order). The values of air density and dynamic viscosity chosen for the simulation correspond to those for 70,000 ft. For analysis at the two

Table 6. Ansys Fluent settings

Variable	Setting
Solver	Pressure-based, Incompressible
Time	Steady
Turbulence model	k-kl-ω RANS
Pressure-Velocity coupling	Coupled
Gradient	Least squares cell based
Pressure	Second order
Momentum	Second order upwind
Turbulent kinetic energy	Second order upwind
Laminar kinetic energy	Second order upwind
Specific dissipation rate	Second order upwind
Air density	0.0709 kg/m^3
Dynamic viscosity	1.4398×10^{-5} kg/m/s
Laminar kinetic energy	1×10^{-6}
Turbulence intensity	0.1%
Turbulent viscosity ratio	1

Reynolds numbers of interest (100,000 and 250,000) the inlet velocities were set as 20.3 m/s and 50.75 m/s, respectively. Due to the low turbulence conditions at such altitudes, the turbulence intensity and turbulent viscosity ratio were set at 0.1% and 1, respectively. The 'prevent reverse flow' was used on the outlet in the event that the far-field domain size chosen introduced back flow.

4.2. Aerodynamic performance at Re = 100,000

A drag polar comparison of the unstructured mesh results, along with an XFOIL baseline and the empirical data of Ref. 8, for Re = 100,000, is presented in Figure 8a. The empirical data in Figure 8a displays the characteristic 'high-drag knee' described by Giguere and Selig [14]; this is a result of the formation and growth of an LSB. The Fluent prediction captures this 'drag-knee' behaviour reasonably well though appears to under-predict the recovery at higher incidence angles. Ref. 9 reports that a bursting LSB can lead to a considerable loss in lift and result in stall, which could explain why the coefficient of lift predicted by Fluent continues to increase over that of the empirical data after 9-degrees. This may be because the LSB remains intact in Fluent, which is further supported by the lack of low drag recovery when compared with both the empirical and XFOIL data. It is apparent from Figure 8a that the deformed aerofoil demonstrates a

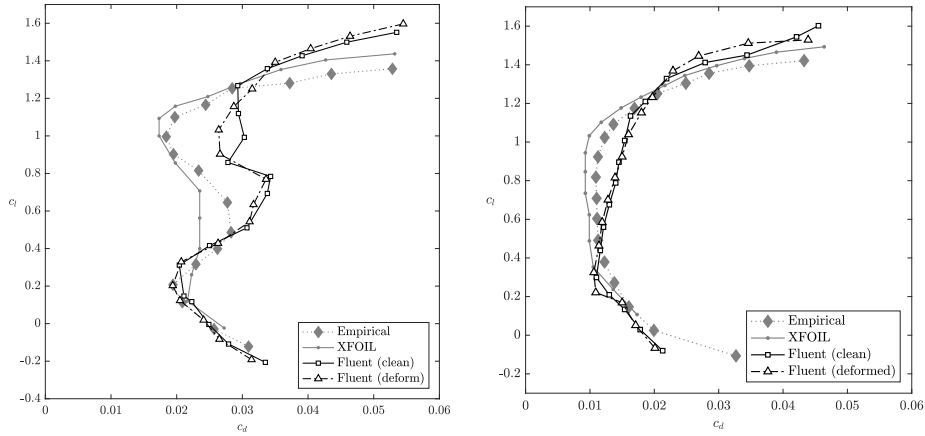

(a) Re = 100,000. **(b)** Re = 250,000.

Figure 8. SG6042 drag polar comparison with Fluent unstructured mesh, XFOIL, and empirical data from Ref. 8.

minor reduction in drag compared to the clean configuration at low values of c_l, which is in line with the expectations of a delayed transition or reduction in size of the LSB.

Figure 9 shows three plots offering a detailed analysis of the flow behaviour within the boundary layer of SG6042 at the Reynolds number of 100,000 and 6 degrees angle of attack. As expected, given the similar curves in Figure 8a, the pressure plots of the clean and deformed aerofoils are very similar (given that the lift produced can be indicated by the pressure distribution). From Figure 9 it is clear that flow separation (identifiable where $C_f < 0$) begins around 30% of the chord on the clean aerofoil, where the pressure gradient levels off over the upper surface of the aerofoil. Shortly after, at around 50% chord, the flow begins to transition; this aligns with a sharp increase in the turbulent kinetic energy (TKE). The transition to fully turbulent flow is realised when the TKE sharply rises to a peak just before 65% chord. Notably, from the skin friction plot of Figure 9c the flow can be seen to fail to reattach to the aerofoil, due to the low-speed flow.

An earlier transition occurs with the deformed aerofoil, which is consistent with the behaviour of a turbulator. This is evidenced by the earlier rise of TKE after 30% chord, a lower plateau in the turbulent kinetic energy at 60% of the chord, and is supported by Figure 10, where there is an appreciable difference in the TKE contours of both the clean and deformed aerofoils. The early transition leads to a small LSB at around 35% of the

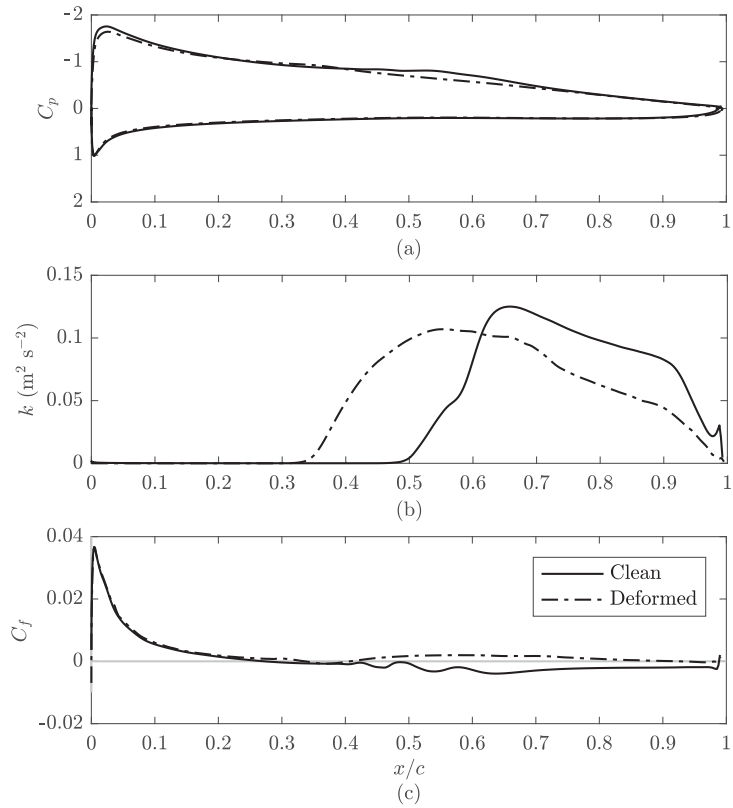

Figure 9. SG6042 plots, at Re = 100,000 and 6° of (a) pressure coefficient, C_p, (b) turbulent kinetic energy, k (upper surface), (c) skin friction coefficient, C_f (upper surface).

chord instead of the flow separating. The deformity is thus behaving like a turbulator in temporarily re-energising the laminar boundary layer. The y^+ value remained below one for the entire aerofoil surface, increasing the confidence that can be had in the results.

Overall the effect of the deformity at Re = 100,000 is very minimal in terms of any change in lift, though does generally provide a minor increase. Similarly, with respect to the drag polar, Fluent predicts a minor improvement. This is due to the prevention of the flow separation, which offsets the drag increase as a result of the minor blockage presented by the deformity. Note that this would not account for any cross flow that may occur in the 3D case.

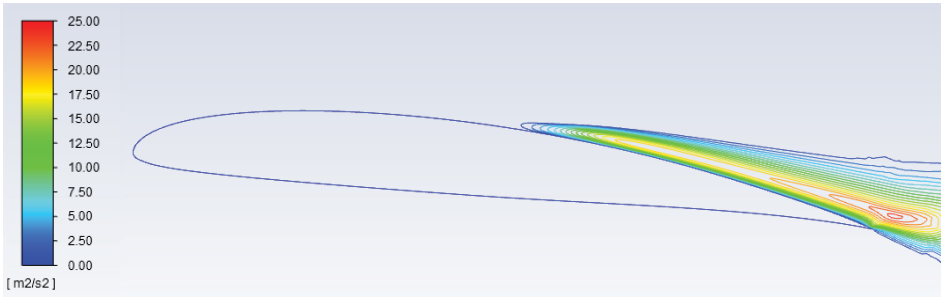

(a) Clean.

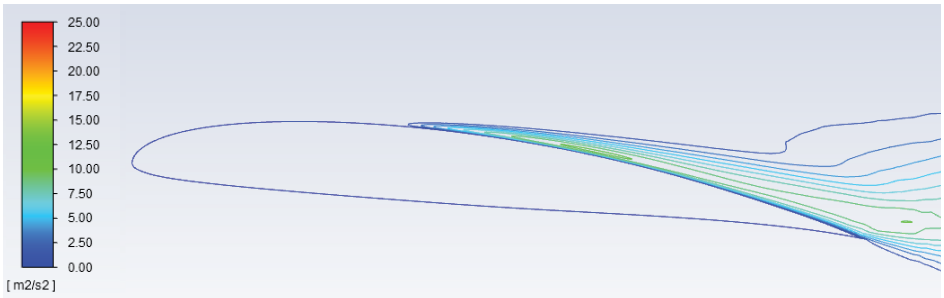

(b) Deformed.

Figure 10. SG6042 turbulent kinetic energy contours (Re = 100,000, $\alpha = 6^{\circ}$).

4.3. Aerodynamic performance at Re = 250,000

In contrast with the performance predicted by Fluent at Re = 100,000, Figure 8b shows Fluent now has much better agreement with the empirical data, for both the deformed and clean configurations at the aerofoil's ideal lift coefficient of 0.6. This is because the high-knee drag associated with the LSB, which dominated this portion of the drag polar, is no longer seen. The performance benefit of the deformity is, however, not as evident at this Reynolds number. The characteristic flattening along the C_p plot, indicative of LSB formation, is no longer present (Figure 11) and the TKE plots in Figure 12 show more similarity, with a LSB appearing to form in both cases (Figure 11c). The formation of the LSB for the deformed foil appears to be marginally delayed by about 5% of the chord and would appear to be of comparable size of that on the clean aerofoil.

It should be noted however that at this Reynolds number the y^+ value at the leading edge and for the first 5% of the chord was greater than 1. This may result in the k-kl-ω model being unable to resolve the boundary layer before the deformity. However, the

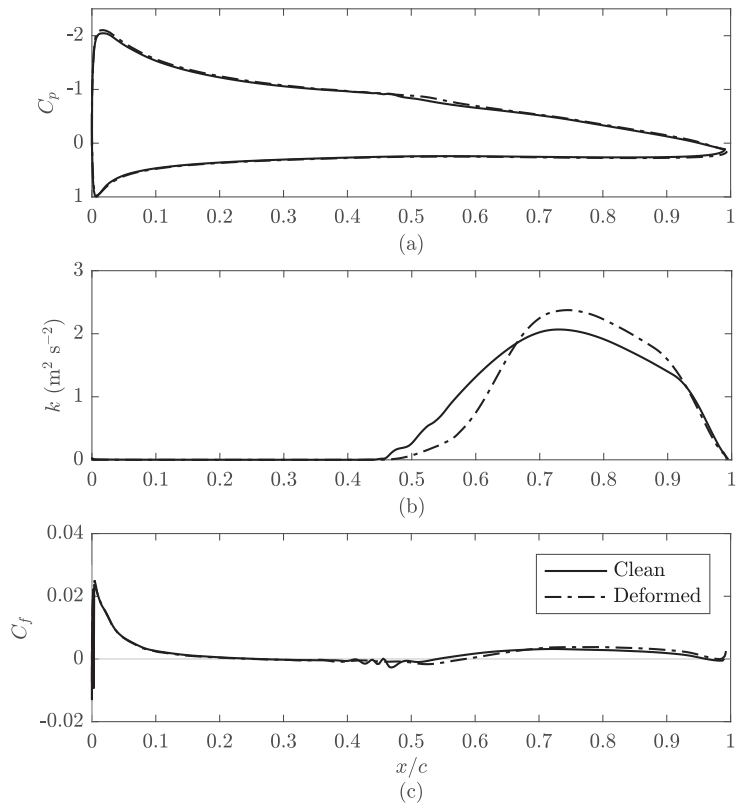

Figure 11. SG6042 plots, for Re = 250,000 and 6°, of (a) pressure coefficient, C_p, (b) turbulent kinetic energy, k (upper surface), (c) skin friction coefficient, C_f (upper surface).

y^+ value did fall below 1 for the rest of the aerofoil surface, suggesting that the model would accurately capture downstream effects.

4.4. Remarks

Ultimately, the 2D deformities were modelled in a similar way to analysis of the effects of trips described by Lyon et al.[8] and behave comparably to them. Fluent predicts the general trend in performance of the deformed aerofoil to offer a net drag reduction at Reynolds numbers of both 100,000 and 250,000 with a deformity height of 0.056% chord. Plots of the minimum power condition ($c_l^{3/2}/c_d$) show the optimal cruising angle between 6 and 8, as expected for the SG6042 aerofoil. The minimum power condition

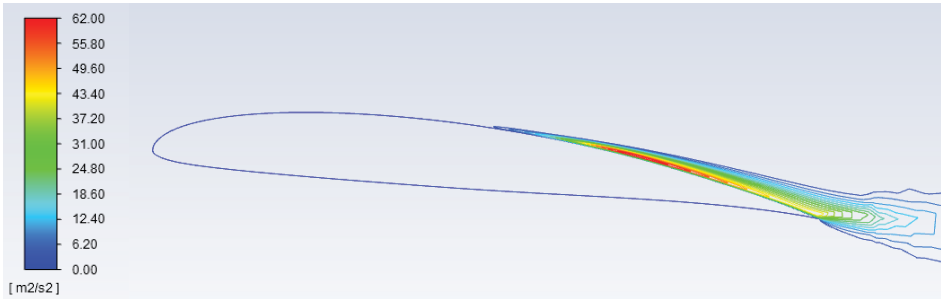

(a) Clean.

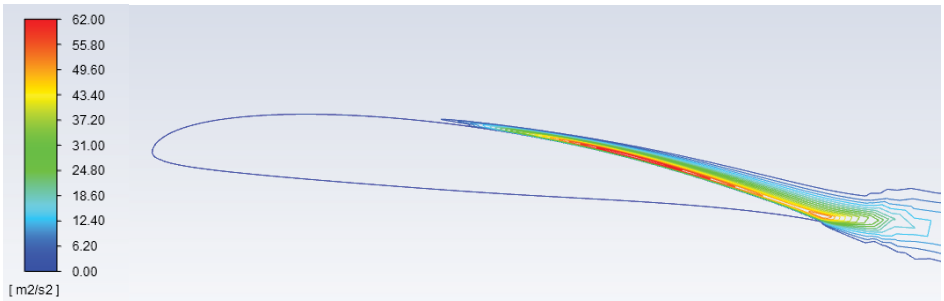

(b) Deformed.

Figure 12. SG6042 turbulent kinetic energy contours (Re = 250,000, $\alpha = 6^{\circ}$).

at a fixed cruising angle is reduced by 8.8% at Re = 100,000 and about 7.2% at Re = 250,000 (Figure 13), suggesting a small loss in the power efficiency for the operation of the HAPS UAS at the desired cruising angle of attack. However, this is based purely on 2D analysis so an in-depth study in 3D would be needed to draw a final conclusion, as suggested in Ref. 31, due to the 2D simulations being incapable of capturing 3D vortex structures and span-wise flow interactions.

No change in the flow conditions over or around the deformity were detected in Fluent with a 0.056% chord deformity. Lyon et al.[8] found that a deformity height greater than 0.04% chord at Re = 300,000 or higher results in a performance loss on the SG6042. This suggests that at Re = 250,000 with a larger deformity height, some flow variation should be observed. Therefore, a cursory investigation of how the deformity height effects the downstream flow was undertaken. A series of simulations were carried out with a variety of deformity heights at Re = 100,000 and 0° angle of attack. Figure 14 shows the downstream wake field from the deformity at three different deformity heights. It is evident that as the deformity height is increased from 0.056% chord,

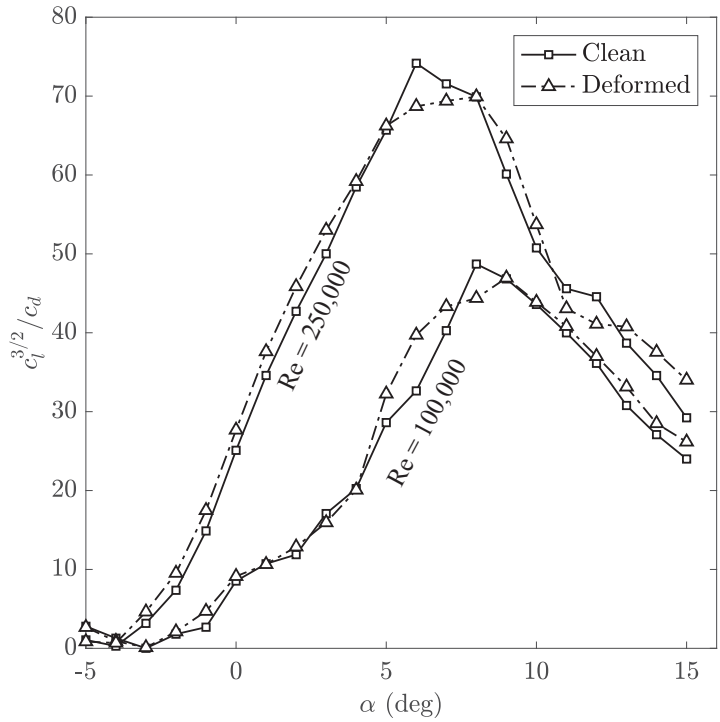

Figure 13. Plot of minimum power condition $\left(c_l^{3/2}/c_d\right)$ for clean and deformed SG6042 aerofoil.

Fluent detects a vortex which grows with increasing deformity height. It can therefore be reasoned from the 2D data, that the deformity height of 0.056% chord is too small to produce downstream vortices and, as such, there would be no significant changes in flow behaviour near the deformity.

5. Comparison with experimental results

5.1. Setup

A closed return wind tunnel at the University of Hertfordshire was used to compare with the CFD method, with a primary objective of flow visualisation and a secondary objective to collect physical test data on a clean and deformed wing for later comparison. For this testing a GOE 523 aerofoil was used.

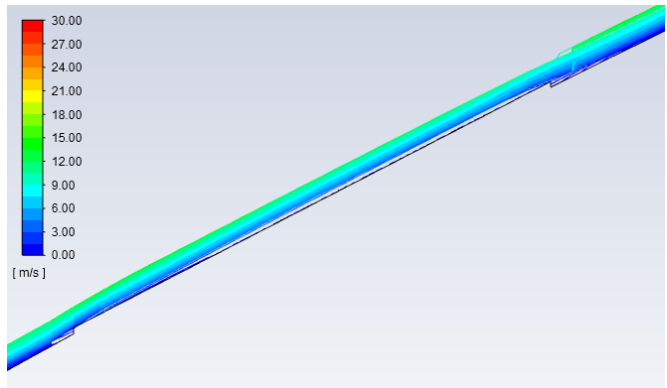

(a) 0.056%.

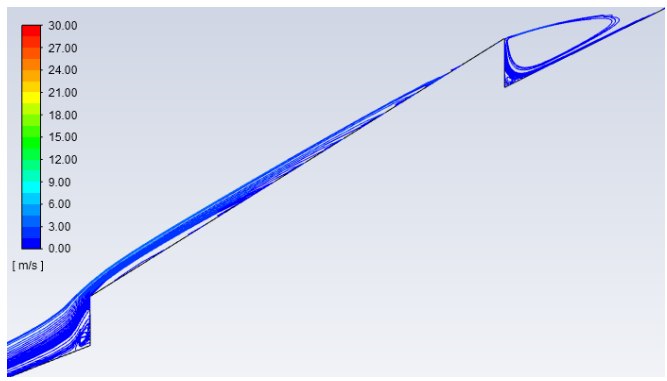

(b) 0.5%.

Figure 14. Wake field (velocity magnitude) around the ridge deformity at different ridge heights (percentage of the chord).

The tunnel has a working section of 1.194×0.84 m^2 and, with the GOE 523 installed, had a blocking ratio of 4.1%. The turbulence intensity of the tunnel, measured using a hot wire anemometer, is approximately 0.1% at a flow speed of 20 m/s but increasingly larger at lower speeds. This is potentially in the region of 1% and higher below speeds of 10 m/s. The tunnel has a three-component, Ate AEROTECH external platform balance arrangement capable of measuring lift, drag, and pitching moments to, typically, $\pm 0.15\%$ full scale.

Figure 15. GOE 523 model mounted in the wind tunnel working section. The position of a smoke injection for visualisation is also indicated.

The GOE 523 aerofoil was first baselined in its clean configuration (Figure 15) with no deformities at the two Reynolds numbers investigated. Given

$$\mathrm{Re} = \frac{\rho V c}{\mu},$$

and assuming sea level values for density and viscosity, the appropriate tunnel velocity for the desired test Reynolds number can be derived from the expression

$$V_{\mathrm{test}} = 1.46075 \left(\frac{\mathrm{Re}}{c} \right) \times 10^{-5},$$

where c must have units of metres. Based on the model's chord length of 0.5 m, at Re = 100,000 and Re = 250,000 the corresponding wind tunnel test speeds were 2.91 m/s and 7.27 m/s. Once the model was mounted in its clean configuration the tunnel balance was zeroed and an incidence angle sweep (from -5 to 15 degrees) was performed three times for each of the Reynolds numbers to get a three-set average.

Once the clean wing tests were finished the deformities were applied. The deformities were created using 0.016 mm thick aluminium foil and adhered to the wing section with removable tape. Due to the small dimensions involved, it was not feasible to physically model the deformity to the chord ratio set out in Table 1. The original

Table 7. GOE523 ridge deformity characteristics.

Characteristic	$\%c$	(m)
First occurrence	10.0	0.050
Separation	17.0	0.085
Height	8.0	0.040
Width	0.4	0.002
Length	0.4	0.002

deformity dimensions were therefore scaled up to enable the replication with the time and materials available. The actual dimensions produced (Table 7) led to the resulting deformity being largely unrepresentative of the original transposition in percentage-chord terms. However, this still enabled some comparison and validation of the CFD methodology.

The deformity was formed by folding the foil in on itself while leaving a flap free either side to tape down, with the aim of presenting a flat face to the flow as described in the previous section. The three ridges were then applied to the GOE 523 wing section to deform it from its clean configuration before mounting in the wind tunnel (Figure 16). The same testing regime as the clean configuration was then carried out.

Drag measurements from the sting and strut supports alone were also made and removed from the aerofoil drag measurements. However, no corrections were made for any interference effects from the struts.

Fluent was setup following the same approach detailed in the previous section, using the GOE 523 aerofoil section. The main difference in approach was the modelling of the wind tunnel domain for the boundary wall. A smaller base element size of 0.01 mm was used. Although 60 inflation layers were specified, due to the deformity geometry this was limited to 20 in Ansys' automatic meshing, so this value was used for both clean and deformed aerofoils. Based on the previous mesh size testing, some small error in the magnitude of the aerodynamic coefficient results might be expected, particularly the lift. The turbulence of the tunnel at the tested speeds was assumed to be high so the turbulent intensity and viscosity ratio were set to 5% and 10, respectively. Note that at this condition the accuracy of XFOIL should be considered carefully as its use of e^N transition theory is not valid at such high turbulence levels.

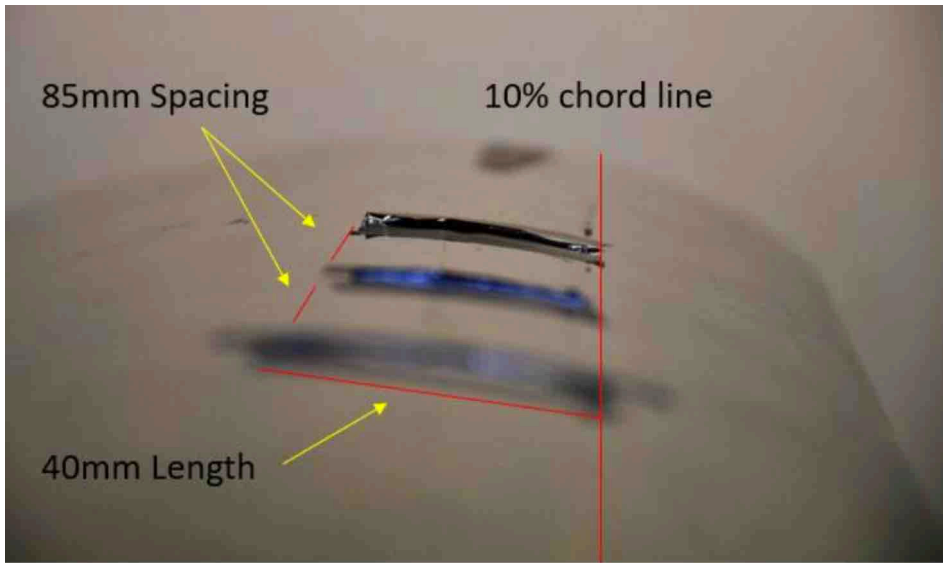

Figure 16. GOE 523 wind tunnel test model with modelled ridge deformities.

5.2. Results

The Fluent and XFOIL results were corrected for aspect ratio, enabling a comparison with the wind tunnel dataset. This is achieved from Prandtl's classical lifting-line theory. For a wing of infinite span then $c_l = a_\infty(\alpha - \alpha_0)$, where a_∞ is the 2D section lift curve slope, dc_l/dα. For a wing of finite span,

$$C_L = a_1(\alpha - \alpha_0) = \left(\frac{a_\infty}{1 + \frac{a_\infty}{\pi A_R}(1+\tau)} \right)(\alpha - \alpha_0). \tag{2}$$

The planform-specific parameter τ is assumed to be negligible. Assuming that α_0, the angle of attack that produces zero lift, is the same in both 2D and 3D cases then $(\alpha - \alpha_0) = c_l/a_\infty$ and

$$C_L = \left(\frac{a_\infty}{1 + \frac{a_\infty}{\pi A_R}(1+\tau)} \right) \frac{c_l}{a_\infty} = \frac{c_l}{1 + \frac{a_\infty}{\pi A_R}}. \tag{3}$$

For the most part, the GOE 523, SG6042, and other high-lift sections have relatively high lift curve slopes, approaching the theoretical thin aerofoil value of 2π. Taking $a_\infty = 2\pi$

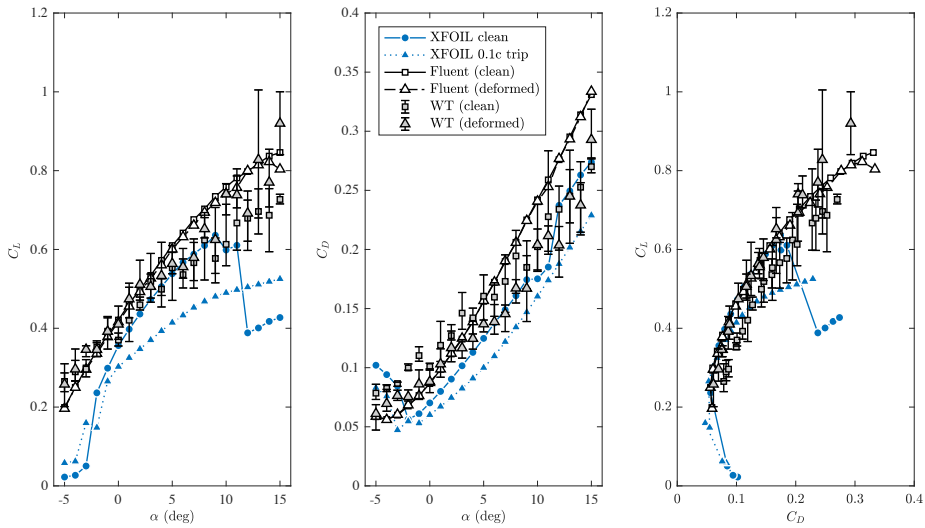

Figure 17. Lift and drag results for the GOE 523 model at Re = 100,000, showing wind tunnel (WT), Fluent, and XFOIL results.

reduces (3) to

$$C_L = c_l \left(\frac{A_R}{A_R + 2} \right). \tag{4}$$

The 2D (profile) drag coefficients are then added to the estimated induced drag,

$$C_{D_i} = \frac{C_L^2}{\pi e A_R}, \tag{5}$$

where the span efficiency factor, e, is estimated[32] (see Ref. 33) as:

$$e = 1.78(1 - 0.045 A_R^{0.68}) - 0.64, \tag{6}$$

giving approximately 1.

Figure 17 shows lift and drag plots comparing GOE 523 data acquired in Fluent, XFOIL, and the averaged wind tunnel (WT) data for the two Reynolds numbers investigated. Although there is some agreement in the magnitude of the values obtained providing confidence in the comparison at these angles of attack, the significant variation in the wind tunnel results makes this comparison hard to verify. The significant variation in the experimental results will be due to the high levels of turbulence at this speed,

in addition to the general poor sensitivity of the load cells at this range. Generally speaking, the WT data (based on the means) suggests that the application of the ridge deformities along the aerofoil have increased the generation of lift compared to the clean configuration. This is the opposite behaviour seen when comparing both the Fluent and XFOIL data, where the deformed or tripped aerofoil has reduced performance in both lift and drag. When comparing XFOIL and Fluent data with that of the wind tunnel it is important to note that, in a 2D model, the deformity is essentially entirely along the span. Whereas, the wind tunnel test model is 3D with three, finite width deformities that may act as vortex generators, producing crossflow redistributions of the momentum throughout the local boundary layer[34].

The deformation appears to maintain the value of the local lift curve slope of the aerofoil whereas the gradient of the clean configuration lift data can be see to slowly decrease. The interesting point here is that although the deformity on the WT model begins at 10% chord, there is not a significant drop in the lift coefficient compared to the clean configuration, suggesting that transition is not occurring at or over the deformity and is likely occurring further downstream. This is supported by the XFOIL 10% trip data, where there is a significant drop in the production of lift to almost half of that seen in the deformed Fluent and WT data. This further implies that the deformity is not triggering transition at 10% chord, which would result in a loss of lift.

Both the Fluent and XFOIL drag results compare well between 0 and 7 degrees angle of attack, following a very similar albeit offsetted drag polar. Whilst both the 2D Fluent deformed and XFOIL 10% trip results showed an increase in drag over their clean counterpart, when the drag is corrected for induced drag as shown, the XFOIL data shows the opposite effect, with the 10% trip providing a noticeable drag reduction. This is consistent with the experimental results, with the clean WT model demonstrating higher drag than the deformed WT model. This may be accounted for by 3D crossflow effects, where the deformity successfully reduces the bubble drag and provides a net drag reduction. Such behaviour is also evidenced in Ref. 8, where a E374(B) aerofoil showed a net reduction in drag at Re = 100,000 with a variety of three-dimensional trip configurations. Interestingly, the difference in drag between the clean and deformed aerofoils from Fluent calculations, when accounting for lift-induced drag, disappear because of the reduction in C_L due to adding the deformity.

At 7 to 8 degrees angle of attack, the XFOIL prediction for the clean configuration begins to shows an increase in drag, followed by a higher spike at 10 to 11 degrees; this corresponds with a sharp fall in lift. During this period the LSB, which started

(a) Clean **(b)** Deformed

Figure 18. Smoke visualisation of separation on the GOE 523 (Re = 100,000, $\alpha = 6°$).

further aft, is moving towards the leading edge (with increasing angle of attack), while the corresponding transition and turbulent reattachment is moving forward on the upper surface of the aerofoil, resulting in nonlinear fluttering in both the lift curve and the drag plot. The laminar bubble itself dramatically increases drag in the local area and this is further compounded by the turbulent reattachment shortly thereafter[8]. The resulting effect is the aerofoil's upper surface being subjected to increasing turbulent separation as the angle of attack increases, thereby increasing drag and reducing lift accordingly. At a Reynolds number of 100,000, it is unlikely that this is due to turbulent transition which suggests that the aerofoil in its clean configuration may be suffering loss of lift due to a large laminar separation bubble.

Figure 18 shows the separation points on the GOE 523 wind tunnel wing section in both clean (Figure 18a) and deformed (Figure 18b) configurations. Notice how the flow separates much earlier on the deformed wing than the clean. This can be seen by the bunching of the smoke within the turbulent flow over the deformed wing compared with the small turbulent flow streak at the trailing edge of the clean wing. However, this difference is not found in the Fluent results.

Figure 19 plots Fluent results from the aerofoil's surface. The deformed aerofoil shows a high peak in suction pressure at the start of the deformity, as seen in Figure 19a. This is generated by the blockage effects caused by the deformity, which then results in an increased localised velocity over the deformity as is evident in Figure 20d. This is substantiated by the work in Ref. 31. At the end of the deformity, the geometry abruptly returns to the curvature of the base aerofoil, deceleration occurs and the flow reattaches shortly afterwards with slightly elevated TKE, which can be seen in Figure 19b and Figure 19c. A LSB then generates later just after 40% of the chord with the separation

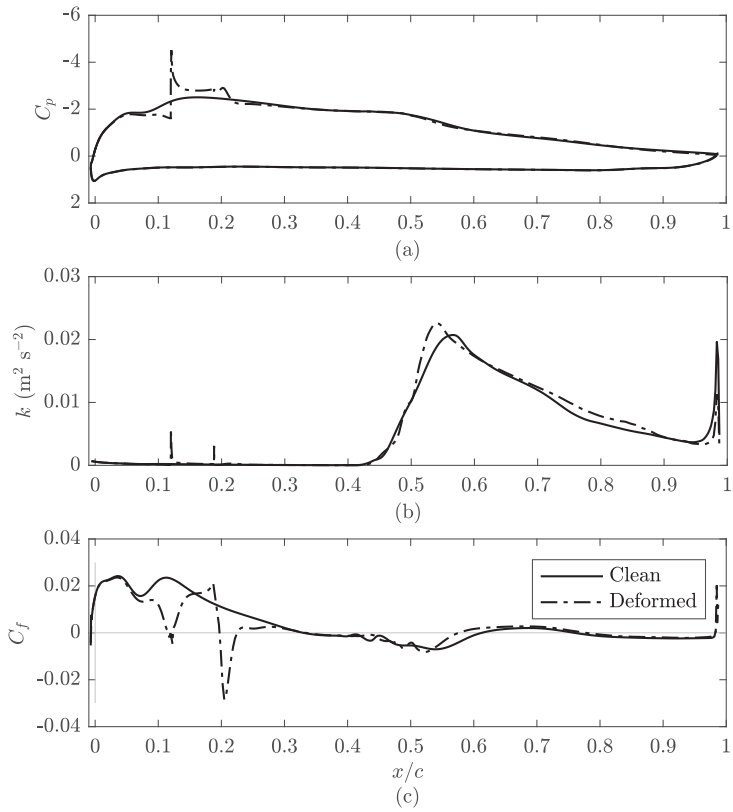

Figure 19. Fluent results of GOE 523 (Re = 100,000 and 6°), of (a) pressure coefficient, C_p, (b) turbulent kinetic energy, k (upper surface), (c) skin friction coefficient, C_f (upper surface).

occurring roughly at the same time as the clean configuration. However, the bubble appears slightly shorter due to the reenergised flow compared to the clean configuration. Ultimately the flow separates in both configurations about 75% of the chord, though marginally later for the deformed aerofoil.

Figure 21 shows C_p plots of GOE523 in XFOIL at three conditions, free transition (clean) and forced transition (tripped) at both 10% and 0.0278% chord. Notice that the flattening of the upper surface pressure distribution correlates with a separation event, be it laminar or turbulent. This can be visualised in the flow path lines around the aerofoil below the pressure plot. By tripping the flow in XFOIL, the solver assumes that the flow is automatically turbulent (after the trip). This differs from the way the deformity works, as at the low Reynolds number regime, in which these aerofoils are investigated, the flow

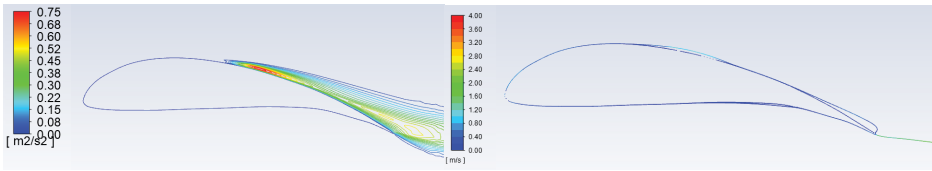

(a) Clean TKE contour **(b)** Clean velocity pathline.

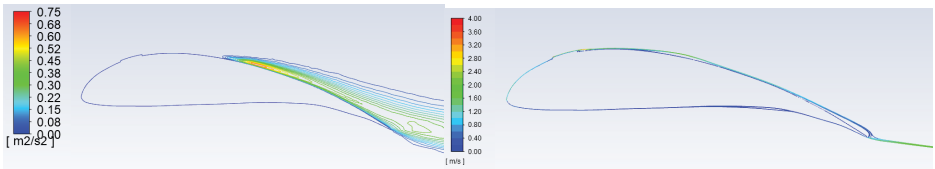

(c) Deformed TKE contour **(d)** Deformed velocity pathline.

Figure 20. GOE 523 Fluent plots at Re = 100,000, $\alpha = 6^\circ$.

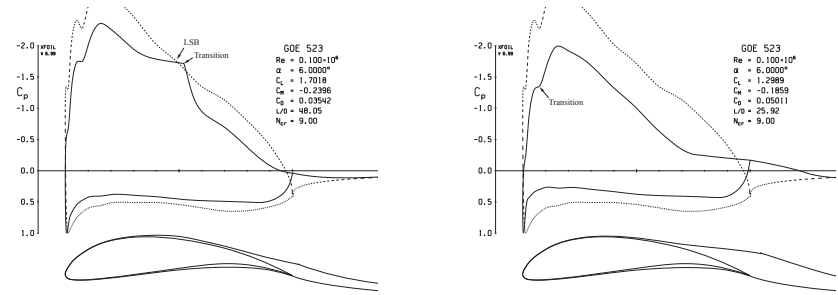

(a) Free transition. **(b)** 10% chord trip.

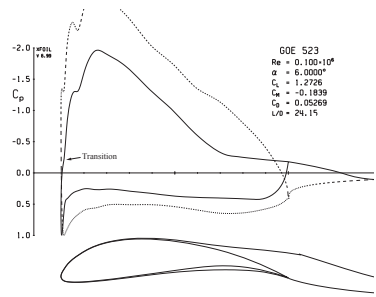

(c) 0.0278% chord trip.

Figure 21. XFOIL GOE 523 pressure coefficient plots (Re = 100,000, $\alpha = 6^\circ$).

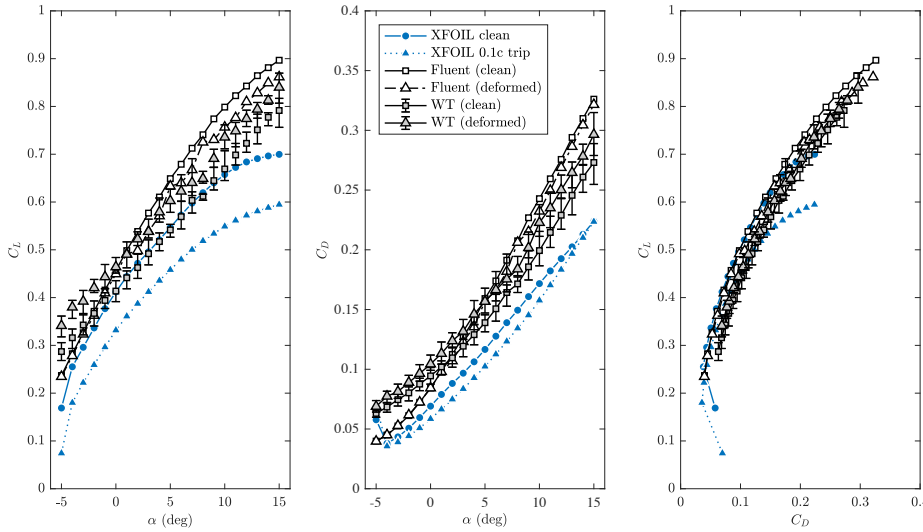

Figure 22. Lift and drag results for the GOE 523 model at Re = 250,000, showing wind tunnel (WT), Fluent, and XFOIL results.

may not become turbulent immediately upon perturbation with the deformity. Hence the tripping of the flow in XFOIL is a guide to correlate data against, as a worst-case situation for comparison. It can be seen that Figure 21b and 21c have very little or no noticeable difference in the pressure distributions nor the boundary layer path line, however, both of these tripped scenarios result in a lift to drag ratio ($L/D \approx 25$) of almost half of that seen in the left plot ($L/D \approx 48$).

Consider now the results for Re = 250,000, shown in Figure 22. The sharp variations in the XFOIL predictions at Re = 100,000 is no longer present in the clean configuration for Re = 250,000. There is now much better correlation of the trend between the three methods (Fluent, WT and XFOIL). XFOIL now accurately predicts the performance of the clean WT model between -1 and 8 degrees angle of attack, with a 0.26% difference at 6 degrees, compared to 6.3% difference at Re = 100,000. The Fluent lift curve over-predicts the clean WT model, especially at the higher angles, which again could be explained by Fluent's overestimate of the persistence of LSBs. However, Fluent appears to more accurately predict the lifting characteristics at higher angles while XFOIL predicts the beginning of a stall at 11 degrees. The Fluent drag results are now better aligned with the wind tunnel results, whereas the XFOIL drag estimates are notably underestimated.

The wind tunnel results at this speed are far more consistent to the extent that clear differences between the two configurations can reliably be seen. As with the results at Re = 100,000 the WT results show a lift benefit obtained by the deformity. However, at Re = 250,000 there is no longer a net drag benefit and instead the drag increases. This is likely due to the deformity position or size not being optimal for Re = 250,000. After correcting for induced drag any difference in drag is still hard to see in the Fluent results (only a very small decrease in drag can be observed at the higher angles) whilst XFOIL still reports a decrease in drag due to the boundary layer trip. Lyon et al.[8] show that the Reynolds number as well as the position and size of a trip effect the net drag and can account for either a benefit or a drawback in performance.

Figure 23 presents results with a behaviour similar to that in Figure 19, though it can bee seen the LSB is much reduced in size and trailing edge flow separation occurs later at 90% of the chord. Figure 24a also demonstrates the shortening of the LSB at Re = 250,000 compared to 100,000. The flattened C_p distribution between 30% to 55% chord in Figure 21a suggest the length of the LSB at Re = 100,000 to be 25% chord, compared to a 15% chord LSB (30 to 45% chord) at Re = 250,000 (Figure 24a), demonstrating LSB reduction with increasing Reynolds number. As with the flow at Re = 100,000 the deformity excites a slightly larger turbulent flow, this time of greater relative magnitude and earlier with the peak occurring at 50% of the chord. However, this turbulence is moderately lower over the aft surface of the foil compared to the clean configuration, whereas in Figure 19b it can be seen to be more or less consistent with the clean configuration. The main difference is the greater amount of turbulence generated aft of the deformity.

5.3. Remarks

The volatility in the wind tunnel results at Re = 100,000 limits meaningful conclusions to be drawn at this test condition with respect to them. However, the general trend in the results were observed at Re = 250,000 with wind tunnel results that where more reliable. The volatility at the lower Reynolds number is explained by the high turbulence in the wind tunnel at this speed. Even at 7 m/s the expected turbulence level most likely exceeds 1%. The similarity in the Fluent results of both clean and deformed configurations, between these two Reynolds numbers, is likely explained by the high turbulence. In fact, previous simulations performed of the SG6024 at this level of turbulence lead to almost indistinguishable behaviour between the clean and deformed foils. This demonstrates the importance of accurate simulation of the turbulence flow conditions at low Reynolds

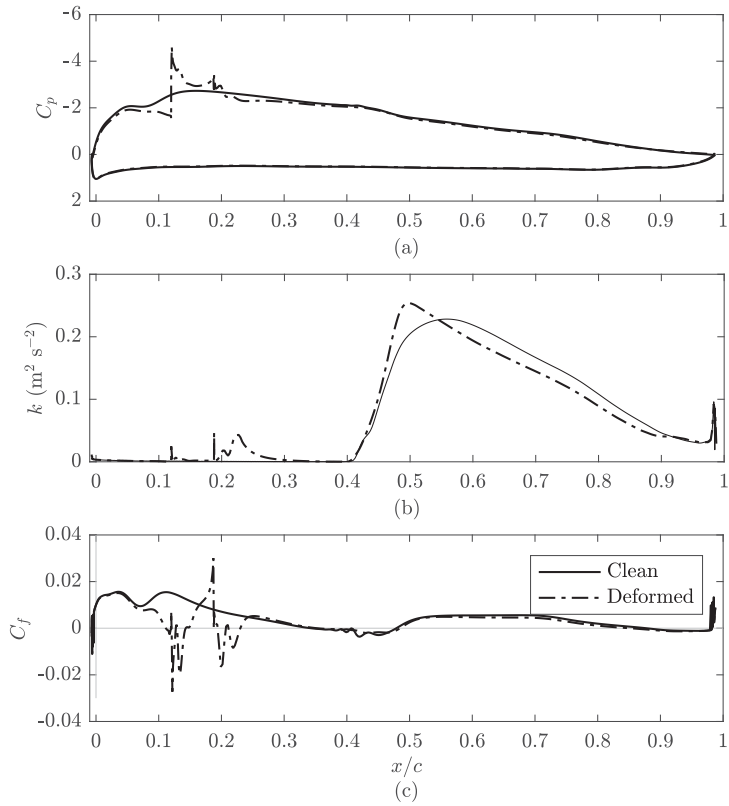

Figure 23. Fluent results of GOE 523 (Re = 250,000 and 6°), of (a) pressure coefficient, C_p, (b) turbulent kinetic energy, k (upper surface), (c) skin friction coefficient, C_f (upper surface).

numbers. This also likely explains the significant difference in magnitude of the lift and drag results seen from XFOIL.

The apparent benefit of the deformity in increasing the lift, as observed in the wind tunnel results, was not observed in either Fluent or XFOIL. The most likely explanation for this is the limitations in the 2D modelling compared to the finite width deformities on the wind tunnel wing. The deformities added to the wind tunnel wing most likely behaved like conventional vortex generators and thus produced some advantage to the lifting behaviour. Such behaviour could not be captured in either Fluent or XFOIL simulations. Thus, whilst the overall aerodynamic performance indicated from the CFD and wind tunnel results was generally agreeable, 3D simulations will be needed to verify the flow behaviour for such large deformities.

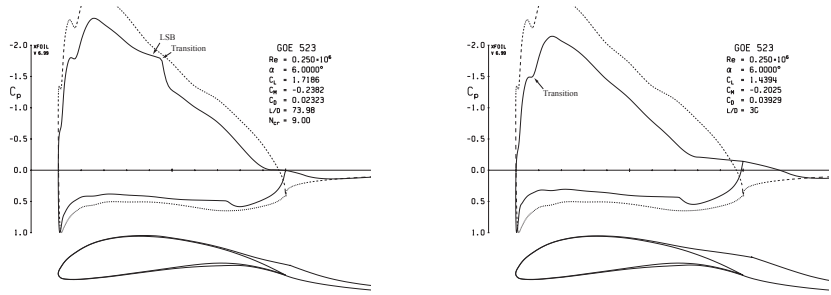

(a) Free transition. **(b)** 10% chord trip.

Figure 24. XFOIL GOE 523 pressure coefficient plots (Re = 250,000, $\alpha = 6^{\circ}$).

6. Conclusions

The extent to which leading-edge deformities affect the aerodynamic performance of an aerofoil within the stratosphere has been studied as a 2D problem, analysing low Reynolds number flow over a clean and deformed aerofoil.

The deformities have been characterised as a function of the aerofoil chord length, enabling scaling to be applied as required. The SG6042 aerofoil profile was modified to include a ridge deformity and imported into Ansys Fluent for CFD analysis. The results showed that the deformity acts very much like a transition trip when modelled in this simple 2D method. Other deformity geometry was deemed not to offer significant differences to the ridge deformity due to the nature of the 2D aerofoil simulation assuming infinite span.

The lift performance of the aerofoil when deformed did not deviate much from that of the clean configuration, to the point of having a negligible impact. There was, however, a net drag reduction associated with the deformed aerofoil, which was attributed to the prevention of flow separation at Re = 100,000 and the delay and shrinking of the laminar separation bubble at Re = 250,000. The deformities did not trip the flow to premature transition but instead re-energised the boundary layer, resulting in the aforementioned effects to the laminar separation bubble. It was not possible to visualise a change in the flow conditions over the deformity when compared with the clean aerofoil. Only when the deformity height was increased was there a significant vortex response observed, suggesting the average deformity height (0.056% chord) seen in production has an insignificant effect on the flow quality at cruise conditions.

Based on the 2D data analysed, the leading-edge deformities will offer a small reduction in drag. However, as a result, there would be a slight shift in the minimum power condition with a decrease in performance at the standard designed values to the order of 8%, due to the small variations in the lift and drag. This would ultimately result in a performance loss for a HAPS UAS in terms of power efficiency and endurance at cruise at the current operating flight condition. In that sense, modelling and compensating for the aerodynamic impact of the deformities is worthwhile. Also, processes to eliminate them from the manufacturing process would be beneficial.

The conclusions from the 2D analysis were not clearly observed in the experimental testing on the GOE 523 aerofoil, which may very likely be explained by crossflow induced by the deformities. The 2D modelling fails to accurately capture the change in the aerodynamic performance of the large deformities on the wing. Their behavioural equivalence was perhaps more akin to vortex generators than to the full-span skin deformations modelled here. The significance of this effect on the transition behaviour possibly explains the difference in the experimental results. Since the transition process caused by such crossflow is more pronounced on swept wings, exploring the effect these deformities have on increasingly swept back wings would also be an area of interest for further study.

Declaration of conflicting interests

The authors declared no potential conflicts of interest with respect to the research, authorship, and/or publication of this article.

Funding

The authors received no financial support for the research, authorship, and/or publication of this article.

Acknowledgements

The authors would like to acknowledge the constructive and insightful comments from the reviewers that have helped in improving the quality of the work.

References

1. Selig M, Donovan J and Fraser D. *Airfoils at Low Speeds*. Virginia Beach, Virginia, USA: H.A, Stokely, 1989.

2. Schawe D, Rohardt C and Wichmann D. Aerodynamic design assessment of Strato 2C and its potential for unmanned high altitude airborne platforms. *Aerospace Science and Technology* 2002; 6: 43–51.
3. Gonzalo J, López D, Domínquez D et al. On the capabilities and limitations of high altitude pseudo-satellites. *Progress in Aerospace Sciences* 2018; 98: 37–56.
4. Cestino E. Design of solar high altitude long endurance aircraft for multi payload & operations. *Aerospace Science and Technology* 2006; 10: 541–550.
5. Selig M, Guglielmo J, Broeren A et al. *Summary of Low-Speed Airfoil Data*, volume 1. Virginia Beach, Virginia, USA: SoarTech Publications, 1995.
6. Marchman J. Aerodynamic testing at low reynolds numbers. *Journal of Aircraft* 1987; 24(2): 107–114.
7. Chang P. *Separation of Flow*, chapter VII - Characteristics of Separated Flow. Oxford: Pergamon Press, 1970. pp. 272–335.
8. Lyon C, Broeren A, Giguère P et al. *Summary of Low-Speed Airfoil Data*, volume 3. Virginia Beach, Virginia, USA: SoarTech Publications, 1997.
9. Jahanmiri M. Laminar separation bubble: Its structure, dynamics and control. Research report, Göteborg: Chalmers University of Technology, 2011.
10. Augustin K, Rist U and Wagnar S. Control of laminar separation bubbles by small-amplitude 2D and 3D boundary-layer disturbances. In *Enhancement of NATO Military Flight Vehicle Performance by Management of Interacting Boundary Layer Transition and Separation*. RTO-MP-AVT-111.
11. Rothan D. *Low Reynolds Number Laminar Separation Bubble Control Using a Backward Facing Step*. MS Thesis, Embry-Riddle Aeronautical University., Daytona Beach, Florida, USA, 1993.
12. Liepmann H and Nosenchuck M. Active control of laminar-turbulent transition. *Journal of Fluid Mechanics* 1982; 118: 201–204.
13. Maestrello L, Bayliss A, Mangalam S et al. Boundary layer transition. In *Langley Symposium on Aerodynamics*, volume 1. Hampton, Virginia, USA, pp. 333–345.
14. Giguère P and Selig M. Aerodynamic effects of leading-edge tape on aerofoils at low reynolds numbers. *Wind Energy* 1999; 2(3): 125–136.
15. Salim S and Cheah S. Wall y^+ strategy for dealing with wall-bounded turbulent flows. In *International MultiConference of Engineers and Computer Scientists, IMECS 2009*. Hong Kong.
16. Ansys Inc. Ansys Fluent, 2019R3 (19.5).

17. Giguère P and Selig M. New airfoils for small horizontal axis wind turbines. *Journal of Solar Energy Engineering* 1998; 120(2): 108–114.
18. Drela M and Youngren H. XFOIL 6.99.
19. Ren K, Hu J, Xiong X et al. Validation of turbulence models in STAR-CCM+ by N.A.C.A. 23012 airfoil characteristics. In *ASEE Northeast Section Conference*. Bridgeport, Conneticut, USA.
20. Zhang W, Cheng W, Gao W et al. Geometrical effects on the airfoil flow separation and transition. *Computers & Fluids* 2015; 116: 60–73.
21. y Lian and Shyy W. Laminar-turbulent transition of a low reynolds number rigid or flexible airfoil. *AIAA Journal* 2007; 45(7): 1501–1513.
22. Balakumar P. Direct numerical simulation of flows over an NACA-0012 airfoil at low and moderate reynolds numbers. In *47th AIAA Fluid Dynamics Conference*. Denver, Colorado, USA.
23. Bose C, Gupta S and Sarkar S. Transition to chaos in the flow-induced vibration of a pitching–plunging airfoil at low reynolds numbers: Ruelle–Takens–Newhouse scenario. *International Journal of Non-Linear Mechanics* 2019; 109: 189–203.
24. Sørensen N, Méndez B, Mũoz A et al. CFD code comparison for 2D airfoil flows. *Journal of Physics: Conference Series* 2016; 753(8): 1–16.
25. Walters DK and Cokljat D. A three-equation eddy-viscosity model for reynolds-averaged navierstokes simulations of transitional flow. *Journal of Fluids Engineering* 2008; 130(12): 121401.
26. Langtry R and Menter F. Correlation-based transition modeling for unstructured parallelized computational fluid dynamics codes. *AIAA Journal* 2009; 47(12): 2894–2906.
27. Langtry R and Menter F. Transition modeling for general CFD applications in aeronautics. In *43rd AIAA Aerospace Sciences Meeting and Exhibit*. Reno, Nevada, USA.
28. Aftab S, Rafie AM, Razak N et al. Turbulence model selection for low reynolds number flows. *PLoS ONE* 2016; 11(14): e0153755.
29. Kožíšek M, F urst J, Příhoda J et al. Implementation of k-kl-ω turbulence model for compressible flow into OpenFOAM. *Applied Mechanics and Materials* 2016; 821: 63–69.
30. Malanthara A and Gerstle WH. Comparative study of unstructured meshes made of triangles and quadrilaterals. In *Proceedings of the 6th International Meshing Roundtable*. Albuquerque, New Mexico, USA, pp. 437–447.
31. Sreejith B and Sathyabhama A. Numerical study on effect of boundary layer trips on aerodynamic performance of E216 airfoil. *Engineering Science and Technology, an International Journal* 2018; 21(1): 77–88.

32. Cavallo B. Subsonic drag estimation methods. US Naval Air Development Center Report NADC-AW-6604, 1966.
33. Raymer DP. *Aircraft Design: A Conceptual Approach*. 2nd ed. AIAA, 1992.
34. Groot KJ, Serpieri J, Pinna F et al. Secondary crossflow instability through global analysis of measured base flows. *Journal of Fluid Mechanics* 2018; 846: 605–653.